Frequency effects on the scale and behavior of acoustic streaming

Michael B. Dentry
Monash University, Clayton, VIC 3800, Australia

Leslie Y. Yeo
Micro/Nanophysics Research Laboratory, RMIT University, Melbourne, VIC 3000, Australia

James R. Friend*
Micro/Nanophysics Research Laboratory, RMIT University, and the Melbourne Centre for Nanofabrication, Melbourne, VIC 3000, Australia

(Received 16 March 2013; revised manuscript received 22 November 2013; published 21 January 2014)

Acoustic streaming underpins an exciting range of fluid manipulation phenomena of rapidly growing significance in microfluidics, where the streaming often assumes the form of a steady, laminar jet emanating from the device surface, driven by the attenuation of acoustic energy within the beam of sound propagating through the liquid. The frequencies used to drive such phenomena are often chosen ad hoc to accommodate fabrication and material issues. In this work, we seek a better understanding of the effects of sound frequency and power on acoustic streaming. We present and, using surface acoustic waves, experimentally verify a laminar jet model that is based on the turbulent jet model of Lighthill, which is appropriate for acoustic streaming seen at micro- to nanoscales, between 20 and 936 MHz and over a broad range of input power. Our model eliminates the critically problematic acoustic source singularity present in Lighthill's model, replacing it with a finite emission area and enabling determination of the streaming velocity close to the source. At high acoustic power P (and hence high jet Reynolds numbers $\mathrm{Re_J}$ associated with fast streaming), the laminar jet model predicts a one-half power dependence ($U \sim P^{1/2} \sim \mathrm{Re_J}$) similar to the turbulent jet model. However, the laminar model may *also* be applied to jets produced at low powers—and hence low jet Reynolds numbers $\mathrm{Re_J}$—where a linear relationship between the beam power and streaming velocity exists: $U \sim P \sim \mathrm{Re_J^2}$. The ability of the laminar jet model to predict the acoustic streaming behavior across a broad range of frequencies and power provides a useful tool in the analysis of microfluidics devices, explaining peculiar observations made by several researchers in the literature. In particular, by elucidating the effects of frequency on the scale of acoustically driven flows, we show that the choice of frequency is a vitally important consideration in the design of small-scale devices employing acoustic streaming for microfluidics.

DOI: 10.1103/PhysRevE.89.013203 PACS number(s): 43.35.+d, 43.38.Rh, 47.61.−k, 77.65.Dq

I. INTRODUCTION

Recently, much interest has been paid to ultrasonic sources as a means to induce fluid motion, known as acoustic streaming, in microfluidic systems [1]. In particular, surface acoustic wave (SAW) transducers operating at O(10–100 MHz) have been demonstrated to generate fast acoustic streaming in small-scale systems [2] such as in drops [3–5] and microchannels [6–9]. Microtechnology exploiting this phenomenon offers a controlled means to generate fluid flow with standard microfabrication techniques and without moving parts. With further advances in the field toward fluid actuation and manipulation at progressively smaller dimensions, motivated by the promise of nanofluidics for manipulation and detection at a single molecule level [10], there is a need to extend the entire suite of SAW microfluidic operations [1] to these smaller scales. The main constraint in achieving SAW fluidic actuation in submicron geometries, however, lies in the SAW wavelength and hence frequency. This was clearly evident in the SAW microchannel experiments of Tan *et al.* [6,11], who demonstrated a strong relationship between the flow characteristics and the channel dimension: unidirectional flow was only achieved in the channel when the channel dimension was comparable to the sound wavelength in the liquid (that, in turn, is dependent on the SAW frequency). It then becomes apparent that higher SAW frequencies must therefore be employed to drive SAW actuation in submicron channels. Nevertheless, there is a lack of fundamental understanding of the effects of frequency on acoustic streaming arising from SAWs. We therefore conducted experiments in a large fluid domain, over a broad frequency range ($\omega/2\pi$ = 20–936 MHz), with the aim of investigating the behavior of the acoustic jet unimpeded by solid boundaries. In particular, we examine the effect of the applied frequency on the geometry and velocity of the jet, and how these play a role in the streaming of the fluid. While others have attempted to account for the effect of frequency $\omega/2\pi$ through the attenuation length over which the SAW decays, α^{-1}, and hence the distribution of energy that is leaked into the fluid [12], we contend (and will show below) that a quantification of the effect of ω on the power density and hence the streaming velocity u necessitates the consideration of the acoustic attenuation length of the sound beam in the fluid, β_u^{-1}, and hence the length scale of the jet, which itself scales as $1/\omega^2$ [13].

More specifically, as a beam of sound propagates through a fluid medium, it is attenuated due to viscous dissipation, relaxation effects, and turbulent fluctuations within the fluid [13,14], giving rise to a body force along its length. In microfluidic systems, this beam must be confined within

*james.friend@rmit.edu.au

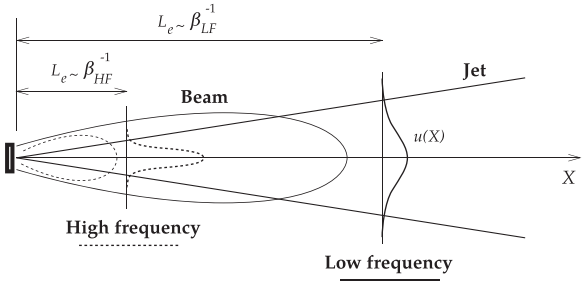

FIG. 1. Schematic depicting the effect of frequency on the attenuation of the sound beam. The cross-sectional area of the streaming jet and the beam length both decrease as the frequency of operation increases, resulting in higher streaming velocities $u(X)$ such that the momentum flux remains constant.

small fluid boundaries, and therefore could be confined in length by the system geometry. The beam attenuation length β_u^{-1}, over which its particle velocity decays by a factor of e, has no effect on the total force applied along the beam, but greatly influences its distribution. Shorter attenuation lengths and higher frequencies have the effect of reducing the total "length" of the beam, thereby increasing its power density. This is illustrated in Fig. 1, where a conical jet of velocity u and radius S generated by a sound beam of constant power is shown at two different frequencies. The "end" of each beam can be defined by the point at which the beam power has decayed to a small fraction of the source power, located at a distance L_b from the source, equal to a few times β_u^{-1} for reasons discussed later. At this point, both jets have the same momentum flux $J = \rho U_e^2 A$ equal to the total acoustic force within the beam, if viscous dissipation can be neglected; ρ is the fluid density, A is the jet cross-sectional area, and $U_e = [(1/A)\iint_A u^2\, dA]^{1/2}$ is the equivalent uniform cross-sectional velocity. For a conical jet, $A \sim S^2 \sim g^2 X^2$, where g is a constant that describes the growth rate of the jet, and hence $U_e(X) \sim J^{1/2} g^{-1} X^{-1}$. Relating the "end" of the beam to the attenuation length $X \sim \beta_u^{-1}$ and noting that $\beta_u^{-1} \sim 1/\omega^2$, we arrive at a relation between the jet velocity and frequency at this point:

$$U_e\left(X = \beta_u^{-1}\right) \sim J^{1/2} g^{-1} \omega^2, \tag{1}$$

revealing the effect of the frequency on the streaming velocity due to the reduction in beam length. Nevertheless, the jet growth S depends on a number of other factors (discussed later) that, together with viscous dissipation of its energy, introduces secondary dependencies on ω.

Here, we revisit the seminal work of Lighthill [14] and rework his model for the growth of turbulent jets to also model the laminar regime, which is more directly relevant to acoustic streaming in small-scale systems at low operating powers, and can be used to predict the behavior of such systems even beyond the transition to turbulent jets, as will be shown later. As high-frequency forcing results in a reduction in the jet length scale (Table I), the necessity to examine the streaming velocity field close to the source also requires us to replace Lighthill's point source with a source of finite area. In what follows, we show that the model we derive is validated by the good agreement between the theoretical scaling predictions we obtain and measurements of the streaming velocity field from our experiments over a frequency range that spans two orders of magnitude. We will, however, first provide a description of our experimental setup in the following section.

TABLE I. Attenuation length of the SAW surface displacement at the $LiNbO_3$-water interface, α^{-1} [Eq. (3)], attenuation length of the sound beam particle velocity in deionized water, β_u^{-1} [Eq. (12)], and characteristic peak velocity location, X_S, for each operating frequency.

$\omega/2\pi$ (MHz)	α^{-1} (mm)	β_u^{-1} (mm)	X_S (mm)
19.7	2.4	120	∼10
54.2	0.87	16	∼6
122	0.39	3.1	∼1
240	0.19	0.80	∼0.5
490	0.097	0.19	∼0.2
936	0.046	0.052	< 0.1

II. EXPERIMENTAL METHOD

Rayleigh SAW devices with frequencies ranging from 20 to 936 MHz were produced by fabricating interdigital transducers (IDTs) comprising straight finger electrode pairs on 127.68° Y-rotated, X-propagating cut, single crystal lithium niobate wafers (Roditi Ltd., London). This was carried out using a standard lift-off technique in which a 60 nm layer of gold was deposited atop a 6 nm chromium adhesion layer. The IDT finger width and gap are each one quarter of a SAW wavelength, i.e., $\lambda_{SAW}/4$; for our 20–936 MHz devices, λ_{SAW} ranges from 196 to 4 μm. The IDTs of the 20–490 MHz and the 936 MHz devices had an aperture of 3.3 and 1.7 mm, respectively. While masking the IDTs, a layer of trichloro(1H,1H,2H,2H–perfluoro-octyl)silane was vapor deposited [15] onto the substrate to force the contact angle of the working liquid (here, we use deionized water) meniscus to close to 90°, measured using side-view microscopy (BXFM Microscope, Olympus, Tokyo) to determine the contact angle. After removal of the masks, the devices were subsequently fixed to a mount and the IDTs were permanently connected to an SMA connector with wire and silver conductive paste. A network analyzer (E5062A, Agilent, Santa Clara, CA) was used to determine the appropriate excitation frequencies of the SAW devices. The SAW vibration velocities generated at each frequency, $\dot{\eta}$, were then measured using a laser Doppler vibrometer (LDV; UHF–120, Polytec GmBH, Waldbronn, Germany). We note that the 490 and 936 MHz devices exhibited a frequency decrease of up to 2% and 7%, respectively, as power was increased; for these devices, the center frequencies were determined using the LDV (as the network analyzer operates at low power), defined as the frequency at which the SAW displacement is at its maximum, suitable for our purposes here [16]. All other devices were found to have a negligible shift in their resonance frequency behavior. To determine the vibration velocity of the SAW $\dot{\eta}$ in each experiment, the maximum vibration velocity $\dot{\eta}_m$ (occurring before contact with the liquid) was measured for each device over the same input power range using the LDV and averaged across the width of the transducer as a function of the voltage. Once in contact with the fluid, the SAW then attenuates along the axis defined

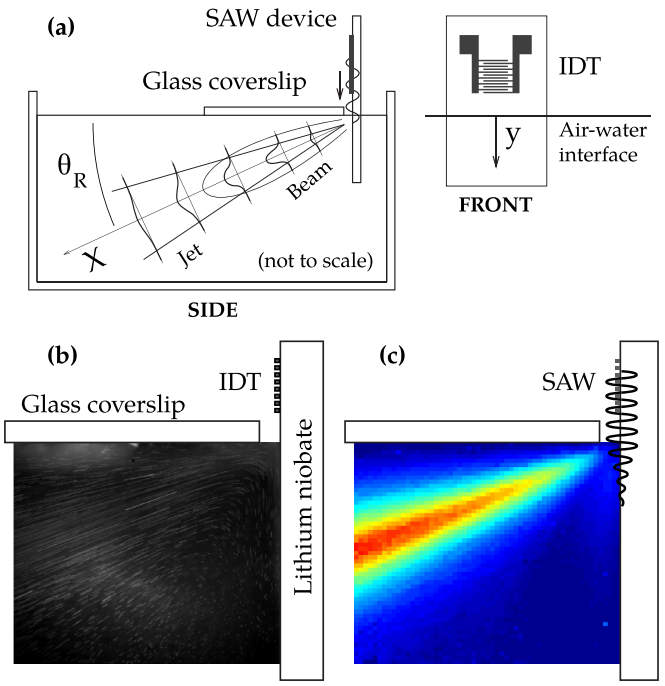

FIG. 2. (Color online) (a) The SAW device was vertically mounted and partly immersed in a water-filled chamber as shown, not to scale, with a representation of the jet that is generated in the chamber. (b) Long exposure image produced from a video of the acoustic streaming at 54 MHz showing the formation of the jet. (c) Corresponding streaming velocity field calculated over an average of 500 frames.

by its propagation direction along the substrate surface y:

$$\dot{\eta} = \dot{\eta}_m e^{-\alpha y}, \tag{2}$$

where

$$\alpha = \frac{\rho c}{\rho_s V_R \lambda_{\mathrm{SAW}}} \tag{3}$$

is the SAW attenuation coefficient [17]. In the above, ρ and ρ_s are the liquid (998 kg/m^3) and substrate (4630 kg/m^3) densities, respectively, c is the speed of sound in the liquid (1498 m/s for water), and $V_R = \lambda_{\mathrm{SAW}}\omega/2\pi$ is the Rayleigh wave phase velocity. We note that the SAW energy leaks into the liquid in the form of planar waves emitted with a wave vector parallel to the Rayleigh angle $\theta_R = \sin^{-1}(c/V_R) \approx 22^\circ$, measured from the axis normal to the substrate surface (Fig. 2). It is this angle that defines the axis along which the sound beam propagates through the liquid. The sound beam within the fluid must have the same frequency as the SAW, and is assumed to have equal particle velocity at the solid-liquid interface, given by Eq. (2). The total power of the sound beam can then be calculated from [17]

$$P = \int_0^\infty \rho w V_R \dot{\eta}^2 dy, \tag{4}$$

where w is the width of the wavefront. In this way, the measured SAW amplitude data can be correlated with the beam power for each streaming experiment, which we describe next.

Briefly, each device was suspended vertically in a glass-walled liquid chamber 75 mm long and 25 mm wide, which was filled with deionized water to within approximately 2 mm of the lower IDT edge (20 mm total depth), as illustrated in Fig. 2; we choose chamber dimensions that are sufficiently large to ensure that the largest jets at low frequencies are unimpeded within the viewing region. A glass coverslip was placed on the air-water interface to maintain a no-slip boundary and ensure that the jet energy is not dissipated through the excitation of capillary waves [18]. The coverslip was placed approximately 1 mm from the device surface to avoid contact and hence interaction with the emanating sound beam. For the 936 MHz device, the coverslip was removed as the jet length became comparable to the gap between the device and the coverslip, and its presence in this case was found to have minimal influence on the streaming velocity measurements.

To visualize the flow, the liquid in the chamber was seeded with 4.8 μm fluorescent polystyrene microspheres—adequately large to avoid Brownian effects and for sufficient light scatter to accurately determine their positions, but not large enough for direct acoustic radiation forces on the particle to overwhelm the drag exerted on the particle [19], important for accurate flow visualization. The particle trajectories were assumed to follow the flow streamlines, based on the supporting observation in the particle tracking results that indicated paths were steady in time and did not cross. The flow was viewed as illustrated in Fig. 2, from the side parallel to both the SAW device surface and the air-water interface; a mercury lamp (Fiber-Lite MH–100, Dolan Jenner, Boxborough, MA) was used to illuminate the flow from above. Each device was connected to a signal generator (SMBV100A, Rhode and Schwarz, Munich, Germany) and amplifier (10W–1000C, Amplifier Research, Souderton, PA) via the SMA cable, with a small connector placed in series to allow for coupling to a voltage probe. A range of input power was applied to each device in this arrangement and the acoustic streaming was recorded with a high speed camera (Fastcam SA–5, Photron, San Diego, CA) at 500–2000 frames/s, chosen to ensure sufficient resolution of the streaming velocity. The camera was connected to a long working distance microscopic lens (K2/SC, Infinity, Boulder, CO), positioned so that the focal plane intersected the central axis of the acoustic jet; the image area captured approximately 8 mm × 8 mm of the flow field. The input power range was limited to ensure that the jet was not disturbed by the effect of the recirculation from the far wall of the chamber.

Each video was analyzed using particle-tracking software (Diatrack, Semasopht, Chavannes, Switzerland) that converted a 500-frame section of each video into an array of displacement vectors for each particle. The array was processed in MATLAB (Mathworks, Natick, MA) to produce a velocity field for each frequency and input power. This was carried out by averaging the displacement vectors at each spatial location and dividing by the time between successive frames. It is then possible to characterize the streaming in each frame by the maximum velocity within the jet, U_S, located on the central beam propagation axis a short distance from the source, X_S.

III. EXPERIMENTAL RESULTS

The long-exposure image shown in the bottom left image of Fig. 2 is a typical representation of the acoustic streaming generated by each of the SAW devices when operated at its

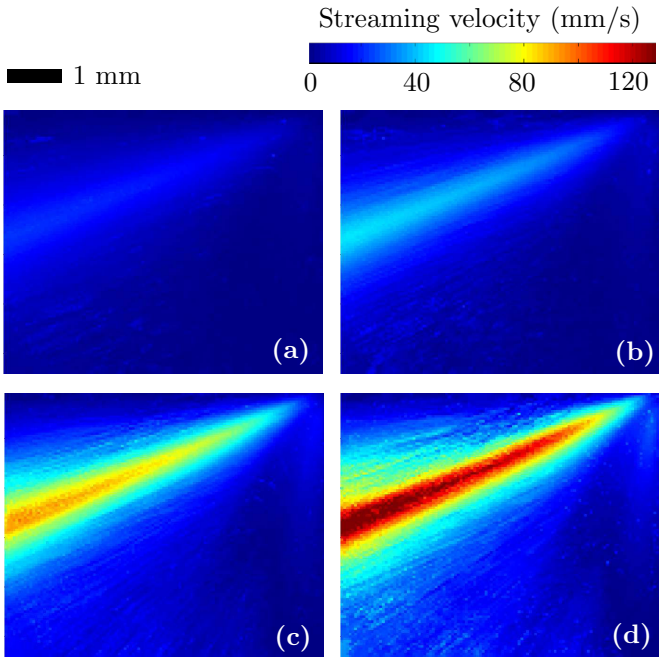

FIG. 3. (Color online) Effect of increasing the beam power on the streaming velocity field for a 54.2 MHz device: (a) 5.8 mW, (b) 17.3 mW, (c) 50.2 mW, and (d) 108.2 mW. The streaming velocity was observed to increase with the beam power, but the flow geometry appeared to be relatively constant.

center frequency. Across the range of frequencies and powers tested, the streaming appears to generally assume the form of a steady jet, of semiangle $\theta \approx 10^{\circ}$, produced within the bulk of the fluid due to the attenuation of the sound beam arising from the acoustic energy leaked into the fluid from the SAW. As the applied power was increased to each device, the streaming velocity is observed to increase, although the flow structure of the jet appeared to remain relatively constant, as shown in Fig. 3. Across different devices with different center frequencies, however, a significant change in the jet geometry was observed, as depicted in Fig. 4.

While the jet structure is observed to be preserved across the range of frequencies, the jet length scale, characterized by X_S, is seen to decrease as the frequency is increased. This is because the attenuation length of the sound beam decreases as $1/\omega^2$, as suggested by the relationship in Eq. (1), thus reducing the beam length and increasing the power density within the jet. We further note that the reduction of scale of the system with increasing frequency also forces recirculation to occur within a smaller localized region closer to the source, thus increasing the jet's velocity and shear stress. This shifts the location of maximum velocity within the jet, X_S, closer to the acoustic source, evident by the characteristic X_S values measured for each frequency in Table I: X_S spans two orders of magnitude. Power was also found to have a smaller effect on the location of X_S, which we shall address later.

We note that beam power governs the total momentum imparted by the jet, and thus the length scale required to diffuse it; therefore, an increase in power extends the total length of the jet beyond the end of the acoustic forcing within the beam (Fig. 5). It does not, however, affect the distribution of

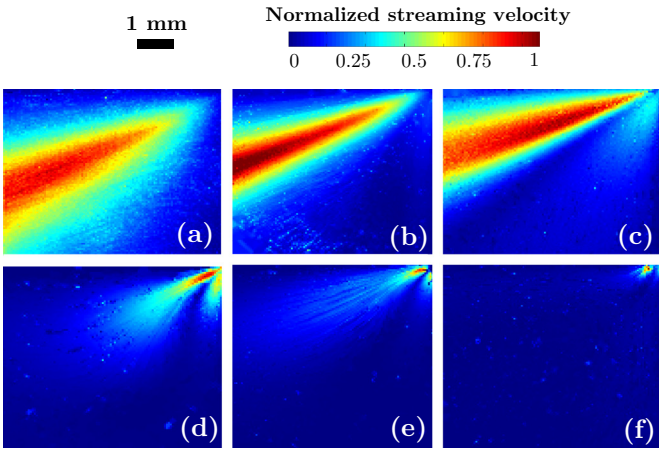

FIG. 4. (Color online) Effect of increasing frequency on the streaming velocity field u, normalized against the maximum streaming velocity U_S: (a) 19.7 MHz, (b) 54.2 MHz, (c) 122 MHz, (d) 240 MHz, (e) 490 MHz, and (f) 936 MHz. The power level for each frequency was selected for each frequency so it was comparable across the frequency range: (a) $U_S = 7$ mm/s, $P = 7.4$ mW; (b) $U_S = 23$ mm/s, $P = 5.8$ mW; (c) $U_S = 47$ mm/s, $P = 2.7$ mW; (d) $U_S = 27$ mm/s, $P = 3.2$ mW; (e) $U_S = 42$ mm/s, $P = 7.5$ mW; and (f) $U_S = 28$ mm/s, $P = 0.8$ mW.

the acoustic forcing as this is solely a function of frequency (when nonlinear effects are negligible), and thus it requires that even at small input powers the length scale of the acoustic forcing is comparable to the beam length. This is shown in Fig. 5, where a beam of low power is compared to one of high power for a constant frequency of 122 MHz: despite the large difference in power between the two cases, the flow is accelerated to maximum velocity over a similar length scale. However, beyond the end of the beam, the streaming within the jet of high power remains strong due to the increased jet momentum.

In all of the cases we examine, the jet is observed to remain nonturbulent, characterized by steady streamlines and low hydrodynamic Reynolds numbers $\mathrm{Re}_s = \rho U_s L/\mu$ of order 1–100, μ being the shear viscosity of the fluid (10^{-3} Pa s) and L the characteristic system length scale (typically 1 mm).

Though Lighthill's model [14] suggests a rapid transition to turbulence from laminar flow as a consequence of the appearance of convective acceleration as a significant component

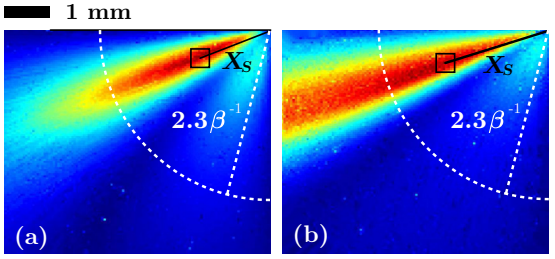

FIG. 5. (Color online) Effect of increasing the beam power on the streaming velocity field for a 122 MHz device: (a) $P \approx 0.1$ mW, $U_S = 6$ mm/s; (b) $P = 3$ mW, $U_S = 47$ mm/s. A radius equal to $2.3\beta^{-1} = 3.7$ mm is shown as an estimate of the end of the beam: the location at which the beam power drops to 1% of the source power.

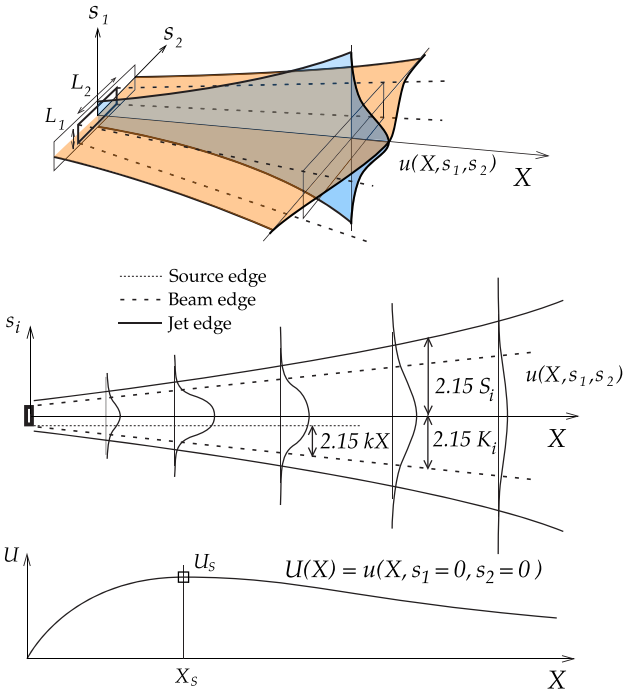

FIG. 6. (Color online) Schematic representation of the geometry of the sound beam and resultant streaming jet. The beam originates from a source of finite area L_1L_2 (in Lighthill [14], a point source is assumed) and grows in dimensions s_1 and s_2 along the beam propagation axis X. Both beam and jet are assumed to have a Gaussian distribution about the central beam propagation axis. Also shown at the bottom is a typical representation of the jet velocity variation along its central axis, along which the beam energy attenuates $U(X) = u(X,s_1 = 0,s_2 = 0)$, showing that U attains a maximum value U_S at a distance from the source X_S before decaying. This is, however, only true for an acoustic source of finite area; as shown in Fig. 7, the jet velocity generated by a point acoustic source does not have a characteristic maximum at some distance but asymptotes to infinity as $X \to 0$.

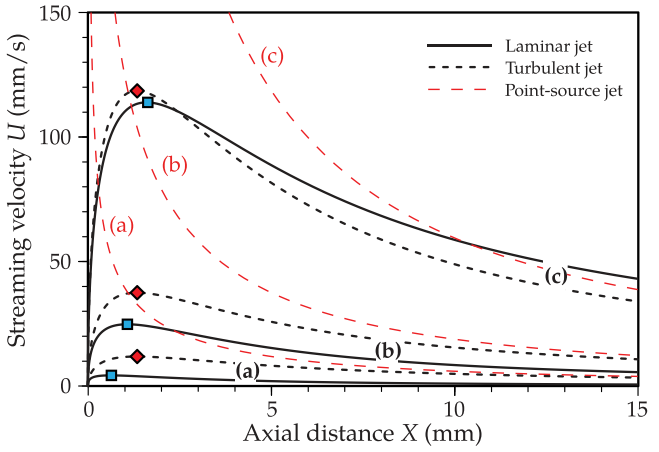

FIG. 7. (Color online) Predictions of the streaming velocity U of the jet along the beam propagation axis X generated by a 100 MHz source for a beam power of (a) 0.1 mW, (b) 1 mW, and (c) 10 mW. The finite area source model predictions are provided as solid black lines for laminar and dotted black lines for turbulent flow. In these models, the jet velocity reaches a maximum U_S at a distance X_S from the source, indicated by blue squares for the laminar jet and red diamonds for the turbulent jet: note how X_S depends upon the input power for the case of a laminar jet but does not for the turbulent jet. Compare these results to Lighthill's turbulent jet model with a point source [14] (dashed red lines): there is no ability to compute the maximum jet velocity U_S in his representation, and the jet velocity near the source grows to infinity.

of the momentum in the jet, we see inertial effects on the flow but no direct evidence of turbulence [20]. This and the necessity to examine the streaming flow field close to the source warrants a modification of Lighthill's model that was derived for a turbulent jet emanating from a point acoustic source; the modified form treats laminar flow from a finite area source. In the next section, we proceed to develop such a model.

IV. THEORETICAL MODEL

A number of forms of acoustic streaming have been investigated since the original work by Rayleigh [21]. These studies predominantly fall within two groups: streaming generated within either the boundary layer [22–24] or in the fluid bulk along the length of an attenuating sound beam, giving rise to a steady momentum flux that is proportional to the applied power [14]. An analytical solution for the latter—the focus of the present work—was developed by Eckart [25], Nyborg [26], Markham [27], and Westervelt [28], constructing a general relationship between the purely oscillatory sound field, and a time-averaged acoustic forcing that drives the steady streaming. The acoustic forcing was identified to be a consequence of Reynolds stress gradients present in an attenuating beam of sound, though the particular solutions derived by the above authors were limited to very slow flows [14].

Lighthill [14], on the other hand, presented a method to calculate the acoustic streaming field generated by high-intensity acoustic fields, taking the form of a turbulent jet. The model assumes a sound beam that originates from a point source and propagates through the liquid to produce an axisymmetric turbulent jet whose spreading, S, along the axis of the beam propagation, X (Fig. 6), can be determined by requiring the energy of the system to be conserved as the beam energy attenuates. The beam width is allowed to grow as kX to produce an axisymmetric fluid jet along the same axis with an assumed Gaussian axial velocity distribution along the radial axis, s:

$$u(s) = \sqrt{\frac{2f(X)}{\pi S^2}} \exp\left[-\left(\frac{s}{S}\right)^2\right], \tag{5}$$

where S is a measure of the jet radius, and $f(X)$ is a function governing the momentum flux of the jet, $\rho f(X)$. We note that the relationship between the jet momentum flux, velocity, and area in Eq. (5) is for a point source and therefore results in a velocity that is singular at the source as $S \to 0$, as shown in Fig. 7: it is only valid some finite distance from the point source. In any case, the beam model is designed to approximate an analytical solution to an otherwise complex acoustic field, requiring numerical solution for each case. A SAW-generated acoustic field is defined by a continuously

decaying vibration amplitude as a boundary condition, caused by the decay of the SAW along the substrate; the emitted waves then also attenuate within the fluid bulk: an acoustic field satisfying these constraints in three dimensions is necessarily complex, as shown in Ref. [29]. Here we apply the beam model approximation to avoid this difficulty, as the small attenuation length of the SAW [$O(1-0.01$ mm)] confines the acoustic energy to a narrow beam close to the source (as shown in Fig. 3 of [29]).

Given the nonturbulent nature of the jets in our study, we modify Lighthill's turbulent jet model [14] to allow application to jets in the laminar regime. This is done by simply exchanging the turbulent dissipation mechanism with one of viscous dissipation. In addition, we extend the model to allow for a finite source area from which the sound energy emanates into the fluid. This is particularly important here as the high-frequency sound fields are confined to very small length scales, generating flows close to the source, and on a similar length scale. The finite source model allows us to examine the streaming velocity in this location. Further, the dimensions of the source area are allowed to be frequency-dependent, and hence proportional to the SAW attenuation length, such that the model is more readily applicable to SAW devices.

We define an orthonormal basis aligned with the axis shared by the beam and the jet, X (defined by the Rayleigh angle, θ_R, Fig. 2), and the lateral axes on which the cross sections of the beam and jet are defined, s_1 and s_2. The acoustic source area is assumed to be rectangular with finite dimensions L_1 and L_2, defined along s_1 and s_2, from which a sound beam with acoustic force per unit volume F, and a fluid jet with velocity u, emanate along X, as illustrated in Fig. 6. In the present case, the geometry of the source is essentially related to the distribution of the SAW on the device substrate: the width of the acoustic source L_2 is constant and approximately equal to the aperture of the IDTs, whereas the source length L_1 is related to the distance over which the SAW decays along the substrate. The power P of the sound beam arising from the SAW energy that is imparted into the fluid is proportional to $\dot{\eta}^2$ from Eq. (4), and therefore the intensity of the SAW decays along the fluid-solid interface (defined along y) as $I \sim \exp(-2\alpha y)$, obtained on substitution of Eq. (2) in Eq. (4). The SAW intensity therefore decays to 1% of the input intensity over a distance $-\ln(0.01)/2\alpha = 2.3/\alpha$; taking the projection of this length on s_1 then allows us to define an acoustic source dimension $L_1 = 2.3\cos\theta_R/\alpha$.

The jet velocity, u, is modified to take the form of a two-dimensional Gaussian along s_1 and s_2, required by the introduction of a rectangular acoustic source of finite area, described by

$$u(s_1,s_2) = \sqrt{\frac{2f(X)}{\pi S_1 S_2}}\exp\left[-\left(\frac{s_1}{S_1}\right)^2-\left(\frac{s_2}{S_2}\right)^2\right], \quad (6)$$

such that the total momentum flux across the jet cross section for constant X is given by

$$\rho f(X) = \rho\int_{-\infty}^{\infty}\int_{-\infty}^{\infty} u^2 ds_1 ds_2. \quad (7)$$

In the above, S_i is a measure of the jet width, differing from that defined in Ref. [14] in that it must account for the finite initial geometry defined by L_i, as shown in Fig. 6. We do this by setting $S_i = S + A_i$, where A_i is a measure of the width of the acoustic source in dimension i (measured from the central axis, i.e., half L_i). For simplicity, we assume that the jet growth S is equal along both s_1 and s_2, i.e.,

$$\frac{dS_1}{dX} = \frac{dS_2}{dX} = \frac{dS}{dX}, \quad (8)$$

on the basis that the fluid medium is homogeneous and isotropic.

As the Gaussian profile extends to infinity along s_1 and s_2, following [14] we define a finite "edge" of the jet where the jet velocity u drops to 1% of its axial value, located on the s_1 and s_2 axes at $s_i = 2.15S_i$, i.e., $\exp(-2.15^2) = 0.01$. We set the edge of the jet at the origin ($X = 0$) *beyond* the edge of the acoustic source, to account for viscous entrainment of flow adjacent to the acoustic beam. This is approximated by defining the initial Gaussian profile such that the point at which the velocity has dropped to 1/2 of its central value is located at the edge of the acoustic source, $s_i = L_i/2$, where the jet has not yet begun spreading (i.e., $S_i = A_i$ as $S = 0$), implying $A_i = L_i/2\sqrt{-\log[0.5]} = L_i/1.67$.

Similarly, the acoustic body force per unit volume, F, within the beam is assumed to take the form of a two-dimensional Gaussian distribution in s_1 and s_2, growing along X:

$$F(X,s_1,s_2) = \frac{\rho f'(X)}{\pi K_1 K_2}\exp\left[-\left(\frac{s_1}{K_1}\right)^2-\left(\frac{s_2}{K_2}\right)^2\right], \quad (9)$$

such that the acoustic force per unit length of the beam, equal to the derivative of the momentum flux, can be specified for constant X as

$$\rho f'(X) = \int_{-\infty}^{\infty}\int_{-\infty}^{\infty} F\, ds_1 ds_2. \quad (10)$$

As with the jet velocity profile, the beam width is related to a factor $K_i = kX + B_i$, describing the growth of the beam kX (here it is linear, as in Ref. [14], and equal in both s_1 and s_2). The edge of the beam is defined as the point at which the acoustic force, F, drops to 1% of its axial value, i.e., $s_i = 2.15K_i$. The beam differs with the jet in that its initial profile at the origin ($X = 0$) is set such that the beam edge is located at the edge of the acoustic source, giving $B_i = L_i/2\sqrt{-\log[0.01]} = L_i/4.3$. For purposes of comparison with the experimental results, we estimate the beam semiangle as $\phi \approx 10^\circ$, approximately equal to that of the jets observed in the experiment. This simplification is justified as ϕ was found to have little influence on the maximum streaming velocity: varying ϕ between 0° and 30° predicts a velocity shift of <10%. The growth rate of the jet is then characterized by $k = \tan\theta_b/2.15$ since $2.15kX = X\tan\phi$.

Given that the momentum flux of the jet, $\rho f(X)$, increases as the sound beam decays along the wave propagation axis, X, we then write

$$f(X) = \frac{1}{\rho c}P[1-\exp(-\beta X)], \quad (11)$$

where P is the power of the sound beam, which can be related back to that of the acoustic source and hence the SAW input power through Eq. (4). The attenuation coefficient of the beam power, β, is equal to twice the value of its

counterpart describing the decay of the particle velocity, β_u, as $P \sim u^2 \sim \exp(-2\beta_u X)$. Therefore, β is given by [30]

$$\beta = 2\beta_u = \frac{b\omega^2}{\rho c^3}, \tag{12}$$

where $b = (\frac{4}{3}\mu + \mu')$, in which μ' is the bulk viscosity of the liquid. The body force in Eq. (9) and the jet velocity in Eq. (6) arising from the momentum flux, $\rho f(X)$, generated from the dissipation of acoustic energy can then be specified.

From [14], the growth rate of the jet can thus be calculated by equating the spatial rate change of the jet energy flux to the acoustic energy influx from the body force given by Eq. (9) minus the rate of viscous shear or turbulent energy dissipation:

$$\begin{aligned}\frac{d}{dX}\int_{-\infty}^{\infty}\int_{-\infty}^{\infty}\frac{1}{2}\rho u^3\, ds_1 ds_2 &= \int_{-\infty}^{\infty}\int_{-\infty}^{\infty} uF\, ds_1 ds_2 \\ &- \int_{-\infty}^{\infty}\int_{-\infty}^{\infty}\mu\left[\left(\frac{\partial u}{\partial s_1}\right)^2 + \left(\frac{\partial u}{\partial s_2}\right)^2\right] ds_1 ds_2. \end{aligned} \tag{13}$$

Substituting the body force and velocity expressions given by Eqs. (9) and (6), respectively, into Eq. (13), and assuming the jet and beam grow equally in both dimensions, as specified by Eq. (8), we then arrive at an expression for the rate at which the jet grows:

$$\begin{aligned}\frac{dS}{dX} &= C\frac{(S_1S_2)^{1/2}}{S_1+S_2}\left(\frac{S_2}{S_1}+\frac{S_1}{S_2}\right) \\ &+ 3\frac{f'}{f}\frac{S_1S_2}{S_1+S_2}\left(1-\frac{2S_1S_2}{\left(S_1^2+K_1^2\right)^{\frac{1}{2}}\left(S_2^2+K_2^2\right)^{\frac{1}{2}}}\right).\end{aligned} \tag{14}$$

For the *laminar* jet model derived above,

$$C = \frac{6\mu}{\rho}\sqrt{\frac{\pi}{2f}}, \tag{15}$$

which contains a dependence on f from substitution of u on the left side of Eq. (13).

In Ref. [14], the turbulent eddy viscosity $\mu_e = 0.016\rho\sqrt{F}$ is, however, used in place of μ in Eq. (13) to account for turbulent dissipation in the jet, and hence the equivalent rate of growth for a *turbulent* jet is simplified through C in Eq. (14) becoming a constant:

$$C_T = [0.016\rho\sqrt{f}]\frac{6}{\rho}\sqrt{\frac{\pi}{2f}} = 0.12. \tag{16}$$

It can be shown that Lighthill's model for the axisymmetric turbulent jet originating from a point source is recovered by setting $A_i = B_i = 0$, which implies $S_1 = S_2 = S$ and $K_1 = K_2 = kX$. Upon setting $C = C_T$ in Eq. (14), the dissipative mechanism becomes turbulent and we obtain the original turbulent jet growth rate in Ref. [14]:

$$\frac{dS}{dX} = 0.12 + \frac{3}{2}\frac{f'}{f}S\frac{k^2X^2 - S^2}{S^2 + k^2X^2}. \tag{17}$$

We note that the laminar dissipation mechanism introduces a factor $f^{-1/2}$ to the otherwise constant growth term in Eq. (14), thus imposing a dependence of S on power, frequency, and position. Solving for the jet profile $S(X)$, it is then possible to determine the velocity along the beam propagation axis (i.e., the maximum velocity of the jet at a given cross section) $U(X) = u(X, s_1 = 0, s_2 = 0)$ from Eq. (6). The resultant velocities for the laminar and turbulent jet models are plotted as black solid and dotted lines, respectively, in Fig. 7. Unlike Lighthill's turbulent jet model for a point source (dashed red lines), which is singular as $\beta X \to 0$, we observe that the velocities in the vicinity of the source remain finite, thus allowing the jet to be analyzed in this region.

The velocities predicted by the different models nevertheless converge far from the source for large βX. More importantly, however, we note the existence of a maximum velocity $U_S \equiv \max_X U(X, s_1, s_2) = \max_X U(X, 0, 0)$ along the beam propagation axis X in the finite source models that is absent in the point source model. In the next section, the existence and amplitude of this predicted maximum velocity are shown to be present in our experimental results. Its existence is due to the competition between the rate at which momentum is added to the jet by the acoustic body force, which increases the jet velocity along its length, and the rate at which the jet dissipates due to viscous and turbulent dissipation [as seen from the loss term in Eq. (13)], which reduces the jet velocity.

V. DISCUSSION

The experimentally measured SAW vibration velocities, $\dot{\eta}$, which are a function of the applied SAW power, facilitate comparison between experiment and theory. Used to calculate the beam power for each experiment from Eq. (4), they predict the spreading of the jet, $S(X)$, from the laminar and turbulent jet models described by Eqs. (15) and (16), respectively, together with Eq. (14). These can then be used to solve for the axial streaming velocity along the length of the jet using Eq. (6). Figure 8 shows a comparison between the experimentally measured and theoretically predicted maximum streaming velocities at X_S, the latter using both laminar and turbulent jet models. Table II shows a comparison of X_S as predicted by theory and measured experimentally for a range of power levels at each frequency, found to be in close proximity. A small increase in X_S is observed when power is increased, but this is dwarfed by the effect of frequency, clearly shown comparing the 54 and 490 MHz devices, the latter having X_S an order of magnitude smaller, for the same beam power. A detailed comparison of the two-dimensional (2D) jet velocity field between theory and experiment for one experimental case is shown in Fig. 9(i), along with the velocity distribution along s_2 in Fig. 9(ii), over three different power levels. The choice of a Gaussian jet velocity profile is validated by reasonably good agreement between experiment and theory, though in all cases there is an expected and observed error in magnitude, originating from the aforementioned theoretical approximations. To further investigate the validity of the Gaussian jet profile, we fit the assumed function directly to the data (shown by the red line).

The differences between the two models and between the turbulent model and the experimental results are especially evident at lower SAW amplitudes, as shown in Fig. 8.

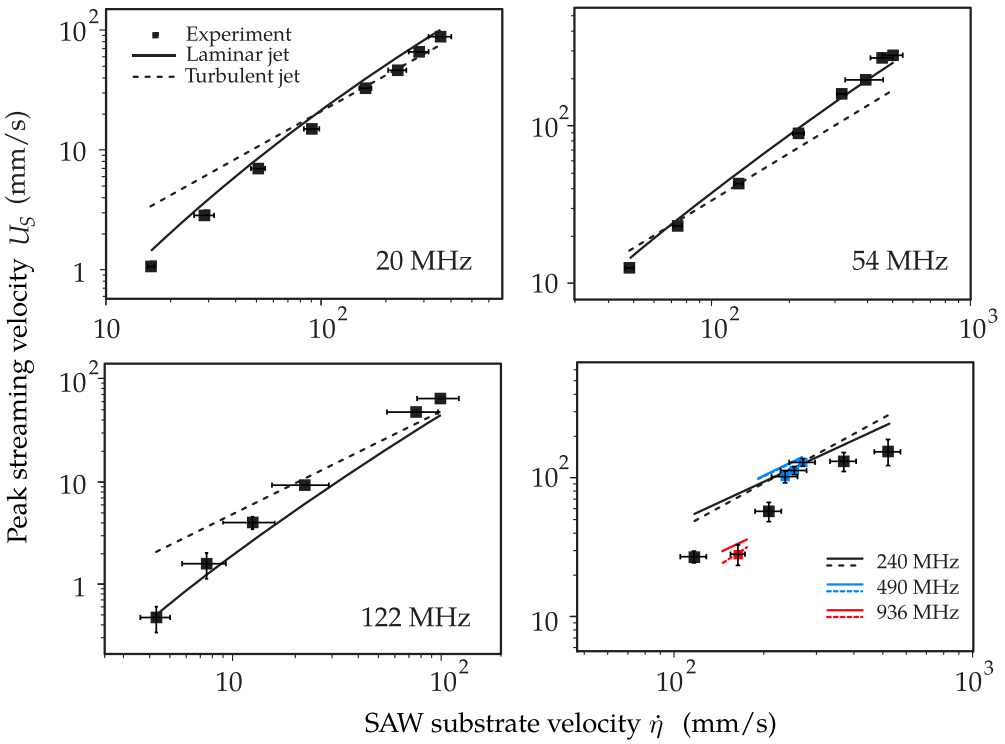

FIG. 8. (Color online) Comparison between the experimentally measured and theoretically predicted maximum streaming velocities U_S as a function of the applied SAW vibration velocity $\dot{\eta}$ for the 20, 54, 122, 240, 490, and 936 MHz SAW devices. Individual points denote the experimental results, while solid and dashed curves indicate the predictions of the laminar and turbulent finite area source jet models, respectively. The 490 and 936 MHz measurements were taken (and calculated) at a distance of approximately 200 μm from the source, as the peak velocity was located too close to the source for accurate measurement. The vertical error bars represent the standard error of the mean in the maximum streaming velocity measurements. For some of the results, the error bars are hidden by the size of the marker, indicating the error is relatively insignificant. The standard error for $\dot{\eta}$ is smaller than the size of the mark used for each data point for all measurements, and hence we instead define the horizontal bars as the standard deviation of $\dot{\eta}$ to illustrate its variation over the width of the IDT.

Good correlation between the laminar jet prediction and the experimental results is found in this range, below a SAW vibration velocity of $\dot{\eta} \approx 100$ mm/s (equivalent to hydrodynamic Reynolds numbers $\mathrm{Re}_s < 100$).

TABLE II. Location of the maximum velocity of the jet, X_S, measured in the experiments, compared with the theoretical prediction for the various frequencies, $\omega/2\pi$, used in the experiment. The peak velocity location for the 19.7 MHz case could not be measured exactly as the total length could not be captured in a single frame, and for the 936 MHz device where the length was too short to accurately determine.

$\omega/2\pi$ (MHz)	P (mW)	X_S (Theor.) (mm)	X_S (Expt.) (mm)
19.7	149–373	16.4–17.3	>7
54.2	6	5.7	6
54.2	17	6.9	6.5
54.2	50	8.2	7
122	0.03	0.7	1.2
122	0.07	0.8	1.3
122	0.20	1.0	1.5
240	3	0.42	0.5
240	10	0.46	0.5
240	32	0.51	0.5
490	4–8	0.13	~0.2
936	0.9–0.6	0.03	<0.1

The dependence of the streaming velocity on the applied SAW power and hence the beam power, related by the SAW substrate displacement velocity through Eq. (4), can be seen in Fig. 10. Here, the power is recast in terms of a dimensionless jet Reynolds number [14],

$$\mathrm{Re_J} = \sqrt{\frac{\rho P}{\mu^2 c}}, \tag{18}$$

evident from a substitution of Eq. (11) in Eq. (15), from which the dissipative function in the *laminar* jet model then becomes

$$C = \frac{6}{\mathrm{Re_J}}\sqrt{\frac{\pi}{2}}[1 - \exp(-\beta X)]^{-1/2}; \tag{19}$$

$\mathrm{Re_J}$ thus captures the relative inertial contribution to the jet through the momentum generated by the sound beam as it propagates through the liquid with the viscous losses due to shear and turbulent dissipation, culminating in the spreading of the jet. Small $\mathrm{Re_J}$ values, therefore, imply viscous dominant jets in which the velocity gradient is smoothed across the flow field due to viscous entrainment of surrounding fluid into the jet, whereas large $\mathrm{Re_J}$ values imply inertial dominant jets in which the viscous entrainment is negligible compared to the convection within the jet, thus leading to high shear

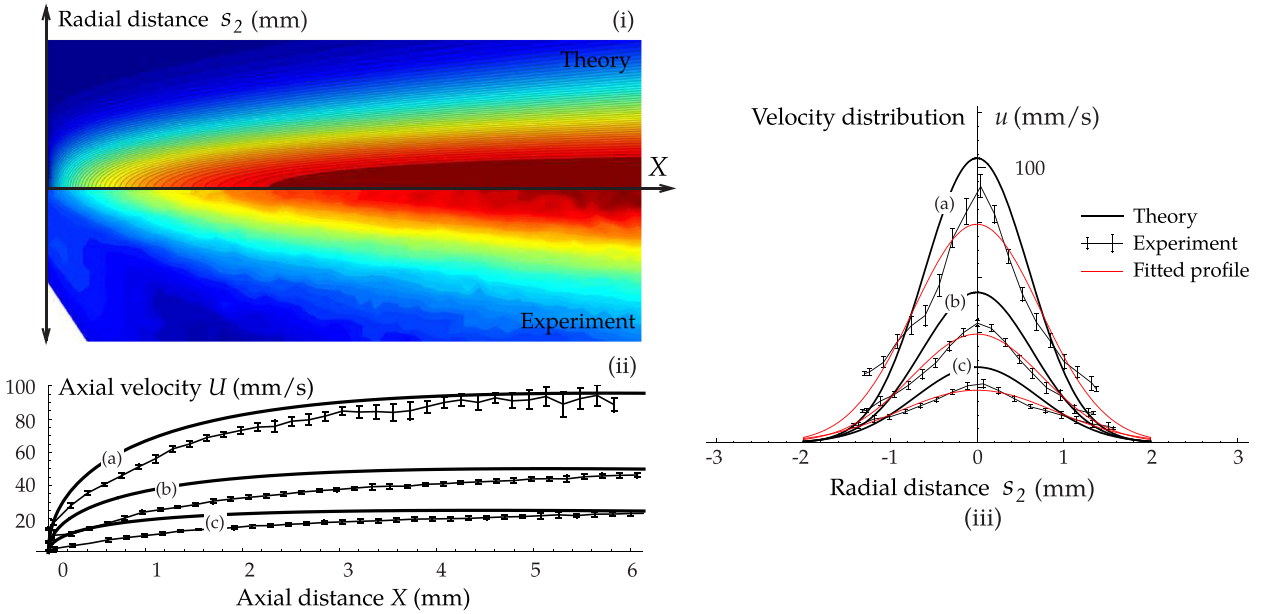

FIG. 9. (Color online) (i) Comparison of the jet velocity distribution between theory (top half) and experiment (bottom half) for the 54 MHz device for a beam power of 17.3 mW, calculated from Eq. (6) at $s_2 = 0$. A comparison of (ii) the axial velocity (at $s_1 = s_2 = 0$) predicted and measured for the 54 MHz device, and (iii) the jet cross-section velocity profile (at fixed X and at $s_2 = 0$) of the 54 MHz device, for increasing input power: (a) 2.5 mW, (b) 5.8 mW, and (c) 17.3 mW. The error bars correspond to the standard error of the measurement ($n > 50$). Fitting a theoretical Gaussian profile to the experimental data (red line) shows reasonable correspondence, justifying the choice of a Gaussian distribution to model the jet.

gradients at the jet periphery. We observe that the turbulent solution for the streaming velocity scales linearly with $\dot{\eta}$ and as $P^{1/2}$ or $\mathrm{Re_J}$, in agreement with [14]. However, the laminar solution does not follow a particular power-law relationship. At low powers, it scales linearly with P or $\mathrm{Re_J^2}$, consistent with observations of slow streaming [31]. At high powers, the scaling of the laminar solution changes, approaching the scaling of the turbulent solution. The limiting behavior between these two power laws arises from the magnitude of the dissipative term—the second term on the right side of Eq. (14); this is governed by $\mathrm{Re_J}$, present in Eq. (19). The streaming velocity, Eq. (6), is proportional to the square root of the momentum flux, $(\rho f)^{1/2} \sim P^{1/2}$, and inversely with the square root of the "area" of the beam: $(S_1 S_2)^{-1/2}$. At high $\mathrm{Re_J}$, the dissipation term is small, and so it exerts little influence on the growth of the jet, $dS\,dX$: the streaming velocity should then be proportional to $f^{1/2}$, which implies it will scale with $P^{1/2}$ for small $\mathrm{Re_J}$. For large $\mathrm{Re_J}$, the viscous term dominates, which implies $dS\,dX \sim C \sim P^{-1/2}$, and therefore $S \sim P^{-1/2}$: an additional dependence on power is introduced. In this case, the jet area becomes power-dependent, $(S_1 S_2)^{1/2} \sim P^{-1/2}$, causing the jet velocity to scale as $u \sim f^{1/2}(S_1 S_2)^{-1/2} \sim P$. This explains the origin of the linear relationship with power observed at low $\mathrm{Re_J}$.

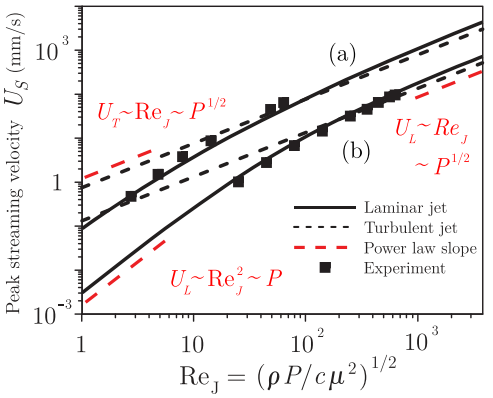

FIG. 10. (Color online) Influence of the beam power P, captured through a jet Reynolds number $\mathrm{Re_J}$ defined by Eq. (18), on the maximum streaming velocity U_S predicted by the laminar and turbulent jet finite area source models at two SAW frequencies: (i) 19.7 MHz and (ii) 121.7 MHz, chosen to represent the phenomenon across the frequencies; the other frequencies provide similar results, although they are omitted here for clarity.

The results in and of themselves cannot be used to determine the transition between laminar and turbulent flow, because the hydrodynamic Reynolds number is too low (1–100) to support such a transition in our system [18]. In fact, Lighthill's computation of a transition to turbulence at a streaming jet $\mathrm{Re_J} = 3.16$ for his particular arrangement [from Eq. (60) of Ref. [14]] does not correspond to the transition from viscous to inertia-dominated flow in either the experimental or theoretical results found in our study, let alone any transition to turbulence, though it is important to remember here the differences in the jets we and Lighthill considered. Here, the change of the scaling of the laminar solution is due to the appearance of convective acceleration of the flow in the jet. However, the power dependence in the relationship between the streaming velocity and input power elucidated by the laminar jet model provides an explanation for the findings of Alghane *et al.* [32], who observed a departure from the linear scaling with power as the power was increased.

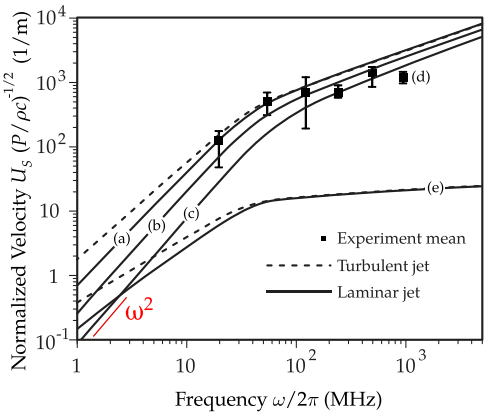

FIG. 11. (Color online) Normalized streaming velocity as a function of the applied frequency for a beam power of (a) 10 mW, (b) 1 mW, and (c) 0.1 mW. The experimental measurements, denoted by the data points, are represented as the average maximum streaming velocity U_S across all power levels at each frequency, with error bars denoting the maximum and minimum power. The experimental data for the 936 MHz device (d) are measured at a distance of 200 μm from the source due to experimental limitations and thus are smaller than the theoretical peak velocity, located at approximately 30 μm. The 10 mW solutions are normalized as $U_S/\sqrt{P\alpha/\rho c}$ in (e), accounting for the effect of the frequency-dependent source area.

The effect of the applied frequency $\omega/2\pi$ on the maximum streaming velocity can be observed in Fig. 11. To clarify the frequency dependence, we normalize U_S by $\sqrt{P/\rho c}$, as apparent from Eqs. (6) and (11), to incorporate its dependence on the beam power. We then observe the normalized streaming velocity $U_S/\sqrt{P/\rho c}$ to scale as ω^2 at low frequencies, in agreement with that predicted by Eq. (1), but approaching a scaling of approximately $\omega^{1/2}$ at high frequencies. Therefore, the commensurate increase in the streaming velocity with increasing frequency is diminished as frequency is increased: for example, doubling the frequency of a 1 mW beam from 20 to 40 MHz results in a 230% increase in U_S, but only a 50% increase when doubling the frequency from 500 MHz to 1 GHz. This behavior is a result of the shortened length of the beam: as frequency is increased, the beam attenuates so rapidly that the jet spreads by only a small fraction of its source dimensions before the beam has decayed entirely, thus having little effect on peak streaming velocity. However, the SAW-emitted beam source area itself is dependent on frequency, through the attenuation length of the SAW on the substrate, $\alpha^{-1} \sim \omega^{-1}$. At high frequencies, where the jet spreading is minimal at X_S, the jet width is highly dependent on the source dimensions; therefore, setting $S_1 \sim \alpha^{-1}$ in Eq. (6) reveals an approximate $\omega^{1/2}$ dependence of U_S, due to the reduction in source area. This scaling is only dominant at high frequency, where the spreading of the jet is small compared to the change in source area. Normalizing U_S against power and the additional factor α^{-1}, i.e., $U_S/\sqrt{P\alpha/\rho c}$, removes this dependency and represents the expected behavior of an arbitrary sound beam emitted from a source area of constant size, shown in Fig. 11(e). In this case, the normalized peak streaming velocity then approaches a constant at high frequency, indicating that for a non-SAW device of constant source area, only a small increase in streaming velocity would be achieved by increasing frequency beyond approximately 100 MHz.

To illustrate the practical implications of these findings, we consider briefly the cost of producing a device versus the benefit of higher streaming velocities as the frequency is increased. Estimating the cost of fabricating such devices is inherently dependent on production rates and desired yields, and is therefore difficult, but a reasonable estimate is to note that the typical output power required for a particular microfluidics application is constant, implying in turn that the size of the device would remain a constant because the electromechanical coupling is likewise fixed. The cost in this case to produce a device increases in proportion to the frequency of the device, because the cost is, roughly, inversely proportional to the minimum feature size used in fabrication [33], and this is, in turn, directly proportional to the wavelength of the SAW. This places Fig. 11 in a new context: the benefit versus cost of increasing frequency is greatest below approximately 100 MHz, beyond which it is reduced. In the case of a fixed acoustic source area (a non-SAW device), fabrication at higher frequencies offers little benefit, as the normalized streaming velocity approaches a constant value.

VI. CONCLUSIONS

We have investigated the effect of the applied frequency on the acoustic streaming generated by SAW devices. Experimental flow visualization by seeding fluorescent particles in the flow field revealed that the streaming generated assumes the form of steady laminar jets that emanate from a source of finite area on the SAW device at the point where it first comes into contact with the fluid. The jets arise as a consequence of the leakage of acoustic energy from the SAW into the fluid at the Rayleigh angle, which subsequently propagates through the fluid as an attenuating sound beam, thereby imparting a nonzero time-averaged momentum flux and hence a body force that drives the flow in the jet. Due to viscous dissipation, the jet spreads laterally, which results in the subsequent decrease in its velocity away from the acoustic source. The length over which the sound beam attenuates then defines the length of the jet, and also plays a significant role in the jet velocity. Given that the beam attenuation length scales as the inverse square of the applied frequency, higher frequencies result in shortened jet lengths and hence increased power densities, leading to faster streaming velocities. As such, a maximum in the streaming velocity will exist at some position along the beam propagation axis before the jet velocity decreases again due to its spreading under viscous dissipation. Unlike previous studies on the effect of frequency on acoustic streaming in small-scale applications that only account for the decrease in the SAW attenuation length scale with increasing applied frequency, we contend that a proper investigation of the effect of frequency necessitates not just a consideration of the attenuation length of the SAW along the substrate under the fluid, as suggested in previous studies [12], but also a careful examination of the attenuation length of the sound beam in the fluid as a function of the applied frequency, and its coupling into the dissipation and spreading of the jet.

We derived a theoretical prediction for the streaming velocity based on the turbulent jet model of Lighthill [14] that accounts for energy conservation in the jet to determine the spreading and hence the velocity distribution within the jet, but with specific modifications to accommodate the high frequency and small-scale SAW system. The infinitesimally small source was replaced with a finite source defined by the size of the SAW aperture and the length scale of the SAW's attenuation *in* the substrate, enabling not only the calculation of the flow field adjacent to the source, but also the prediction of a maximum acoustic streaming velocity and its location for the jet, which were both shown to be consistent with our experimental measurements. The assumption of turbulent streaming was removed, instead employing a laminar jet representation after observing that the turbulent jet model does not accurately determine the streaming velocity at lower excitation powers.

The laminar jet model we derive is validated through the good agreement we observe between the theoretical prediction and experimental measurements of the maximum streaming velocity across a wide range of applied frequencies and SAW powers. At higher powers where the convective acceleration within is relevant, the laminar and turbulent models predict similar streaming velocities. We observe that the model not only captures the correct $U \sim P \sim \mathrm{Re}_\mathrm{J}^2$ scaling and matches the experimentally determined velocities at low powers (or low jet Reynolds numbers), but it also approaches the $U \sim P^{1/2} \sim \mathrm{Re}_\mathrm{J}$ scaling of the turbulent model at high powers (or high jet Reynolds numbers). On this basis, we assert that the laminar model presented here, which accounts for scale-dependent frequency and power effects, is an appropriate model that can be applied to good approximation for predicting the scaling of the acoustic streaming in cases in which the length of the beam is considered to be finite, across low to moderately high Reynolds numbers and across a wide frequency spectrum. Finally, we conclude that the choice of frequency is thus an important consideration for the effective application of acoustic streaming in microfluidic devices, given its significant effect on the geometry and scale of the flow.

ACKNOWLEDGMENTS

This work was performed in part at the Melbourne Centre for Nanofabrication (MCN) node of the Australian National Fabrication Facility, a company established under the National Collaborative Research Infrastructure Strategy to provide nano and micro-fabrication facilities for Australia's researchers. The work was also supported by Australian Research Council Grants No. DP120100013 and No. DP120100835. L.Y.Y. is grateful for funding from the Australian Research Council through an Australian Research Fellowship under Discovery Grant Project DP0985253. J.R.F. is grateful to the Melbourne Centre for Nanofabrication for support through a Senior Tech Fellowship and to RMIT University for support through a Vice-Chancellor's Senior Research Fellowship.

[1] J. Friend and L. Yeo, Rev. Mod. Phys. **83**, 647 (2011).
[2] L. Yeo and J. Friend, Biomicrofluidics **3**, 012002 (2009).
[3] Z. Guttenberg, H. Muller, H. Habermuller, A. Geisbauer, J. Pipper, J. Felbel, M. Kielpinski, J. Scriba, and A. Wixforth, Lab Chip **5**, 308 (2005).
[4] A. Renaudin, P. Tabourier, V. Zhang, J. Camart, and C. Druon, Sensor. Actuat. B-Chem. **113**, 389 (2006).
[5] R. Shilton, M. K. Tan, L. Y. Yeo, and J. R. Friend, J. Appl. Phys. **104**, 014910 (2008).
[6] M. Tan, L.Yeo, and J. Friend, Europhys. Lett. **87**, 47003 (2009).
[7] S. Girardo, M. Cecchini, F. Beltram, R. Cingolani, and D. Pisignano, Lab Chip **8**, 1557 (2008).
[8] L. Schmid, A. Wixforth, D. Weitz, and T. Franke, Microfluid. Nanofluid. **12**, 229 (2011).
[9] S. M. Langelier, L. Y. Yeo, and J. Friend, Lab Chip **12**, 2970 (2012).
[10] R. Mukhopadhyay, Anal. Chem. **78**, 7379 (2006).
[11] M. K. Tan, L. Y. Yeo, and J. R. Friend, Appl. Phys. Lett. **97**, 234106 (2006).
[12] M. Alghane, Y. Q. Fu, B. X. Chen, Y. Li, M. P. Y. Desmulliez, and A. J. Walton, J. Appl. Phys. **112**, 084902 (2012).
[13] J. J. Markham, R. T. Beyer, and R. B. Lindsay, Rev. Mod. Phys. **23**, 353 (1951).
[14] J. Lighthill, J. Sound Vib. **61**, 391 (1978).
[15] N. R. Glass, R. Tjeung, P. Chan, L. Y. Yeo, and J. R. Friend, Biomicrofluidics **5**, 036501 (2011).
[16] A. Meitzler, H. Tiersten, A. Warner, D. Berlincourt, G. Couqin, and F. Welsh III, *IEEE Standard on Piezoelectricity* (IEEE, New York, 1988), pp. 1–74.
[17] J. Cheeke, *Fundamentals and Applications of Ultrasonic Waves*, CRC Series in Pure and Applied Physics (Taylor & Francis, London, 2002).
[18] J. Blamey, L. Yeo, and J. Friend, Langmuir **29**, 3835 (2013).
[19] P. Rogers, J. Friend, and L. Yeo, Lab Chip **10**, 2979 (2010).
[20] C. Thompson, A. Mulpur, V. Mehta, and K. Chandra, J. Acoust. Soc. Am. **90**, 2097 (1991).
[21] L. Rayleigh, Philos. Trans. R. Soc. **175**, 1 (1884).
[22] H. Schlichting, *Boundary-Layer Theory* (McGraw-Hill, New York, 1955).
[23] J. Stuart, J. Fluid Mech. **24**, 673 (1966).
[24] O. Manor, L. Yeo, and J. Friend, J. Fluid Mech. **707**, 482 (2011).
[25] C. Eckart, Phys. Rev. **73**, 68 (1948).
[26] W. L. Nyborg, J. Acoust. Soc. Am. **25**, 68 (1953).
[27] J. J. Markham, Phys. Rev. **86**, 497 (1952).
[28] P. J. Westervelt, J. Acoust. Soc. Am. **25**, 60 (1953).
[29] J. Vanneste and O. Bühler, P. R. Soc. A-Math. Phys. **467**, 1779 (2011).
[30] D. Royer, E. Dieulesaint, and D. Morgan, *Elastic Waves in Solids I: Free and Guided Propagation*, Advanced Texts in Physics (Springer, Berlin, 2000).
[31] A. Nowicki, T. Kowalewski, W. Secomski, and J. Wójcik, Euro. J. Ultrasound **7**, 73 (1998).
[32] M. Alghane, B. X. Chen, Y. Q. Fu, Y. Li, M. P. Y. Desmulliez, M. I. Mohammed, and A. J. Walton, Phys. Rev. E **86**, 056304 (2012).
[33] C. Mack, *Fundamental Principles of Optical Lithography: The Science of Microfabrication* (Wiley, New York, 2011).